Journal of Electronic Materials (2023) 52:3947–3962
https://doi.org/10.1007/s11664-023-10387-w

ORIGINAL RESEARCH ARTICLE

One-Pot Construction of Porous WO_3/g-C_3N_4 Nanotubes of Photocatalyst for Fast and Boosted Photodegradation of Rhodamine B and Tetracycline

Haoran Qian[1] · Jingmin Lu[1] · Lei Ge[1] · Zhongcheng Zhang[1] · Jian Zhang[3] · Zezhong Xu[1] · Shufen Wang[1,2] · Tingting Yu[1,2] · Hongdian Lu[1] · Kunhong Hu[1] · Minghua Li[1,2] · Jinsong Xie[1,2]

Received: 1 December 2022 / Accepted: 14 March 2023 / Published online: 6 April 2023

Abstract

WO_3/C_3N_4 porous nanotubes (WO_3/CNNT) with direct Z-scheme heterojunction have been developed through an effortless one-pot calcination self-assembly strategy. The synthesized WO_3/CNNT heterojunction structure is different from conventional bulk g-C_3N_4 according to field-emission scanning electron microscope (FE-SEM), transmission electron microscope (TEM), and X-ray photoelectron spectroscopy (XPS) spectra analysis, and has a better performance in photocatalytic degradation of pollutants. It is under a unique structure with an elevated interfacial area and high dispersion active sites, which can facilitate the degradation of some dye pollutants and antibiotics by heterojunctions, higher than that of bulk g-C_3N_4 and hollow g-C_3N_4 nanotubes. The photocatalytic experimental results indicated the optimum photocatalyst of the 2% WO_3/CNNT sample with a BET surface area of 108.8 m^2/g, which can rapidly remove Rhodamine B (RhB) and tetracycline (TC) up to 97.4% and 87.4%, respectively, under visible-light irradiation, which was about 3.4 and 83.8 times higher than that of individual CNNT and WO_3 for RhB degradation. Additionally, the degradation of TC was around 1.1 and 14.3 times superior to that of individual CNNT and WO_3. Furthermore, the porous WO_3/CNNT heterojunction turned out to be stable and reusable after four cycles of experiments. Reactive free radical trapping experiments confirmed that holes (h^+) and superoxide ($\cdot O_2^-$) radicals are the most dominant species during photodegradation. Finally, a possible Z-scheme catalytic mechanism is proposed. In this work, some new insights are provided to design novel Z-scheme g-C_3N_4-based heterojunction photocatalysts with a porous nanotube structure and enhanced photocatalytic performance for high-efficiency degradation of dyes and antibiotics.

✉ Jinsong Xie
xjs153@hfuu.edu.cn

[1] School of Energy Materials and Chemical Engineering, Hefei University, Hefei 230601, People's Republic of China

[2] Anhui Provincial Engineering Research Center for Green Coating High-Performance Additives, Hefei University, Hefei 230601, People's Republic of China

[3] Anhui Provincial Laboratory of Biomimetic Sensor and Detecting Technology, West Anhui University, LuAn 237015, People's Republic of China

Graphical Abstract

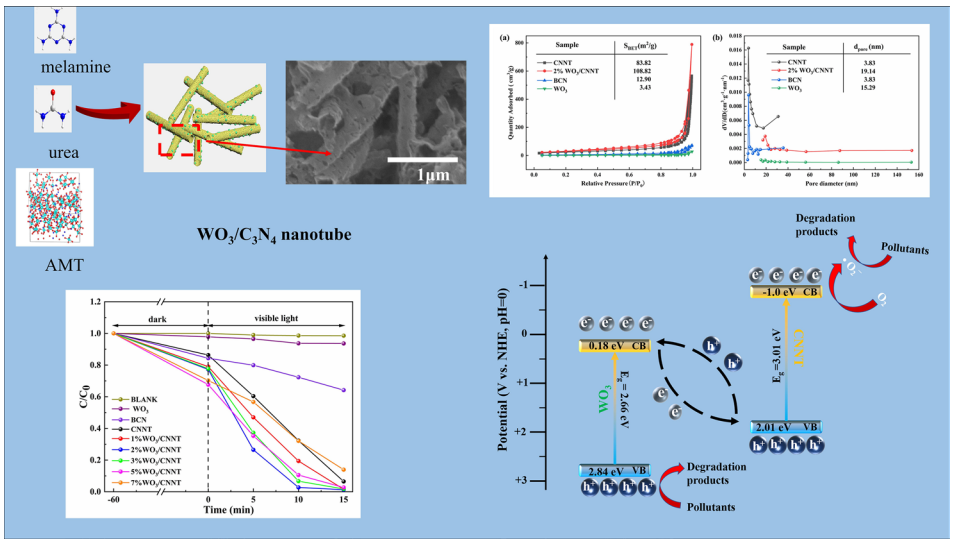

Keywords WO_3/g-C_3N_4 · nanotubes · heterojunction · Rhodamine B · tetracycline

Introduction

Organic pollutants (such as dyes[1–3]) and antibiotics [(including aminoglycoside, β-lactam, glycopeptide, and tetracycline (TC)][4] in wastewater have brought great harm to the environment and human health.[5] Therefore, the exploration of environmental remediation strategies has attracted more and more attention. Pollutant concentrations can be degraded through conventional adsorption[6] and coagulation[7] techniques in a short period of time, but pollutants can be enriched rather than eliminated. Meanwhile, chemical oxidation[8] requires high costs, while biological degradation[9] takes a considerable amount of time, which is still not satisfactory. Compared with all the other methods, due to the mineralization of organics by highly effective active species generated during semiconductor photocatalysis, this has become the most cost-effective and user-friendly alternative for pollutant removal in waste water.[10]

The selection of semiconductor photocatalysts plays a major role in photocatalysis. Traditional inorganic semiconductor catalysts, such as TiO_2 , cannot efficiently utilize the most visible part of solar energy owing to its wide bandwidth (E_g = 3.2 eV).[11] Therefore, the search for visible light photocatalysts with stable competence is still the investigation core in the field of photocatalysis. In the past few years, several researchers have explored photocatalysts with appropriate band gaps for quite a number of environmental purposes, like wastewater treatment (such as dyes,[12] antibiotics,[13] etc.), photocatalytic hydrogen manufacture,[14] and photocatalytic conversion of carbon dioxide.[15] Among these, graphitized carbon nitride (g-C_3N_4) is a typical metal-free semiconductor polymer composed of C and N elements, which is easy to prepare, is non-toxic, has high chemical stability and thermal stability, and appropriately accurate metal loading capacity.[16,17] Wang's research group in 2009 first used g-C_3N_4 as a visible light photocatalyst, which can being about the photocatalytic decomposition of aquatic hydrogen and oxygen production, realizing the expansion from a traditional inorganic semiconductor to a polymer semiconductor photocatalyst.[18] However, common blocky g-C_3N_4 presents deficiencies, such as limited specific surface area, photogenerated rapid carrier recombination, insufficient absorption of visible light, and low quantum efficiency, leading to defects in its photocatalytic performance.[19] In order to avoid these limitations, various modification strategies have been adopted. In recent years, the construction of heterojunction composites, such as Z-type heterojunction, has attracted the great attention of researchers.[20] There is evidence that various semiconductors can form heterostructures with g-C_3N_4, such as TiO_2,[21,22] V_2O_5,[23,24] Bi-based materials,[25–28] and quantum dots,[29] which are effective in prohibiting the recombination of photo-induced electrons and holes.

As a typical *n*-type semiconductor, tungsten trioxide (WO_3) has received more and more attention due to its narrow band gap (2.6–2.8 eV), which can be a good candidate capable of capturing visible light.[30] To increase its catalytic performance, pure WO_3 must be combined with various other semiconductors to enhance its visible-light photocatalytic efficiency through precisely controlled in situ hydrolysis and a successive polymerization

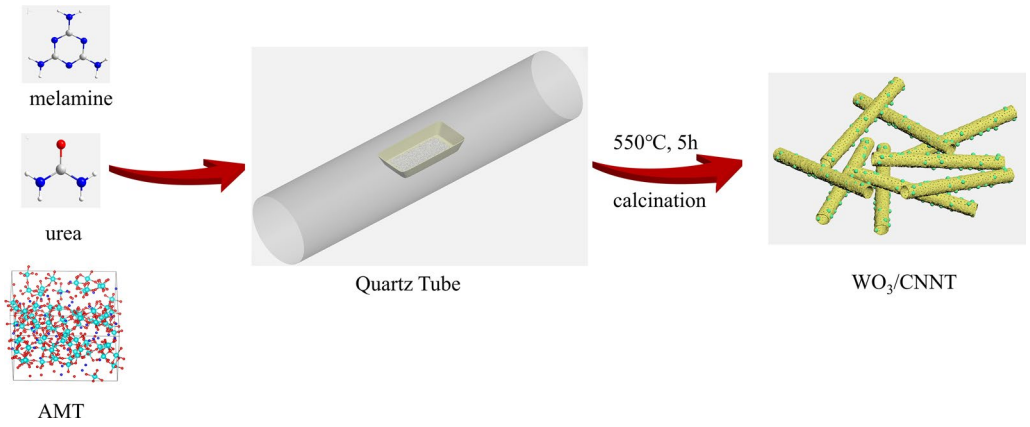

Scheme 1 One-pot calcination of tubular WO_3/g-C_3N_4.

process.[31] For instance, Xiao et al. developed WO_3/g-C_3N_4 composite hollow microspheres, showing enhanced degradation rates against ceftiofur sodium and tetracycline hydrochloride under visible light.[32] Pan et al. synthesized a 2D-2D WO_3/g-C_3N_4 S-scheme heterojunction by a straight forward calcination method, and it displayed more significant photocatalytic performance in TC degradation than WO_3 and g-C_3N_4 under visible-light irradiation.[33] To summarize, based on the advantages of electronic transfer and light absorption between the heterojunctions, the WO_3/g-C_3N_4 composite catalyst can exhibit excellent photocatalytic activity. The nanotubes present a significant advantage in terms of enhancing charge carrier mobility and surface area, but the synthesis process is too time-consuming for widespread production.[34]

In this study, we firstly synthesized a porous WO_3/g-C_3N_4 nanotube heterojunction system by a simple one-pot calcination method, and confirmed its unique porous tubular microstructure by field-emission scanning electron microscope (FE-SEM) and transmission electron microscope (TEM) analysis. The degradation of Rhodamine B (RhB) and TC under visible light and simulated sunlight, respectively, were investigated. Finally, the photocatalytic degradation mechanism of the WO_3/g-C_3N_4 composite is proposed, based on the free radical capture experiment.

Experimental

Materials

Urea (CH_4N_2O; Macklin, 99%), melamine ($C_3H_6N_6$; Macklin, 99%), ammonium metatungstate hydrate ($(NH_4)_6H_2W_{12}O_{40}\cdot xH_2O$; Macklin, 99.5%) were used without purification. Deionized (DI) water was used in the whole experiment.

Preparation of g-C_3N_4, WO_3 and WO_3/g-C_3N_4 Nanotubes

In a typical synthesis process, the nanotubular g-C_3N_4(CNNT) is achieved by placing 4 g urea and 0.4 g melamine in a quartz vessel and heating it at 5°C/min to 550°C for 5 h. Similarly, added melamine was calcined to generate bulk g-C_3N_4 (BCN) for comparison. In the same way, the 2% WO_3/CNNT was synthesized by adding 0.0086 g ammonium metatungstate into the raw materials. Then, 1%, 3%, 5%, and 7% WO_3 -loaded CNNT were obtained by varying the mass of WO_3 under a parallel method (Scheme 1).

Characterization

The X-ray diffraction (XRD) patterns of the materials were observed (D8-Advance; Bruker) with Cu Kα radiation ($\lambda = 0.154056$ nm). Fourier-transform infrared (FT-IR) spectra in the wave-number region of 400–4000 cm^{-1}were obtained (IRAffinity-1S spectrometer; Shimadzu). The produced samples were examined with a field-emission scanning electron microscope (FE-SEM; SU8010; Hitachi) fitted with an energy dispersive x-ray spectrometer (EDS). Transmission electron microscope (TEM) images were obtained (Model 800; Hitachi), and a high-resolution transmission electron microscope (HRTEM; JEM-1230; JEOL). X-ray photoelectron spectroscopy (XPS) spectra were acquired (ESCALAB 250) using monochromatized Al Kα radiation (hv = 1486.7 eV). UV–vis diffuse reflectance spectroscopy (UV–vis DRS) spectra of the samples were acquired (V-650; JASCO, Japan). UV adsorption was tested (UV-1800; MAPADA). To obtain the BET specific surface areas

and pore diameters of the synthetic materials, N_2 adsorption and desorption isotherm tests were conducted (Autosorb-iq; Quantachrome Instruments). To better understand the electrochemical properties, a CHI760E electrochemical system (Shanghai, China) was used.

Electrochemical Performance Measurement

The electrochemical performance was evaluated using a three-electrode system with 0.5 M Na_2SO_4 solution as the electrolyte. The catalyst was coated on 1 cm^2 fluoride-doped tin oxide-coated glass, with half the area immersed in the electrolyte to test its photocurrent transient response. To determine where the conduction and valence bands were located, Mott–Schottky curves were measured at 1 kHz. Furthermore, electrochemical impedance spectra (EIS) measurements were used to determine the charge transfer resistance. The counter electrode (cathode) was composed of a Pt wire, and the reference electrode and the working electrode (photo-anode) were made of Ag/AgCl (saturated KCl).

Photocatalytic Performance Measurement

By degrading Rhodamine B (RhB) and TC in aqueous solutions, the photocatalytic activity of different catalysts was investigated. A RhB solution was prepared with 10 mL 1×10^{-4} mol/L of the original solution and 40 mL DI water. The visible-light source was provided using a 300-W Xenon light (Hxuv300; Beijing CEJ Tech., Beijing, China) and an ultraviolet filter ($\lambda \geq 420$ nm). Prior to the photocatalytic reaction, 10 mg of the catalyst was added to the prepared RhB solution for shading and stirring for 60 min to achieve the adsorption–degradation equilibrium. After that, under continuous visible-light irradiation for 15 min, 5 mL of the suspension was collected and centrifuged at 4000 rpm for 3 min to filter the particles at intervals of 5 min. The photocatalytic property of the WO_3/CNNT composites was also characterized using reactive free radical trapping experiments. Capture agents, ammonium oxalate (AO, 1 mmol), 1,4-benzoquinone (BQ, 0.1 mmol), and dimethyl sulfoxide (DMSO, 1 mmol), 2-propanol (IPA, 1 mmol), were detected as hydroxyl radical ($\cdot OH$), hole (h^+), superoxide radical ($\cdot O_2^-$), and electron (e^-) scavengers, respectively.

The photocatalyst (20 mg) was dispersed in a solution of 50 mL TC at a concentration of 40 mg/L. Adsorption equilibrium was reached by magnetized stirring of the suspension for 1 h in darkness, which was then exposed to simulated solar light (without a filter). A 5 mL suspension was extracted every 20 min, and the granular photocatalyst was derived from aqueous solution using a 20,000-rpm centrifuge. With a UV–vis spectrophotometer, the RhB concentrations and the TC concentrations were respectively measured during the photodegradation process by recording the variations in the absorption bands at 554 nm and 357 nm.

Results and Discussion

XRD Analysis

The XRD patterns of tubular g-C_3N_4 are similar to bulk g-C_3N_4 with two characteristic peaks at $2\theta = 13.5°$ and

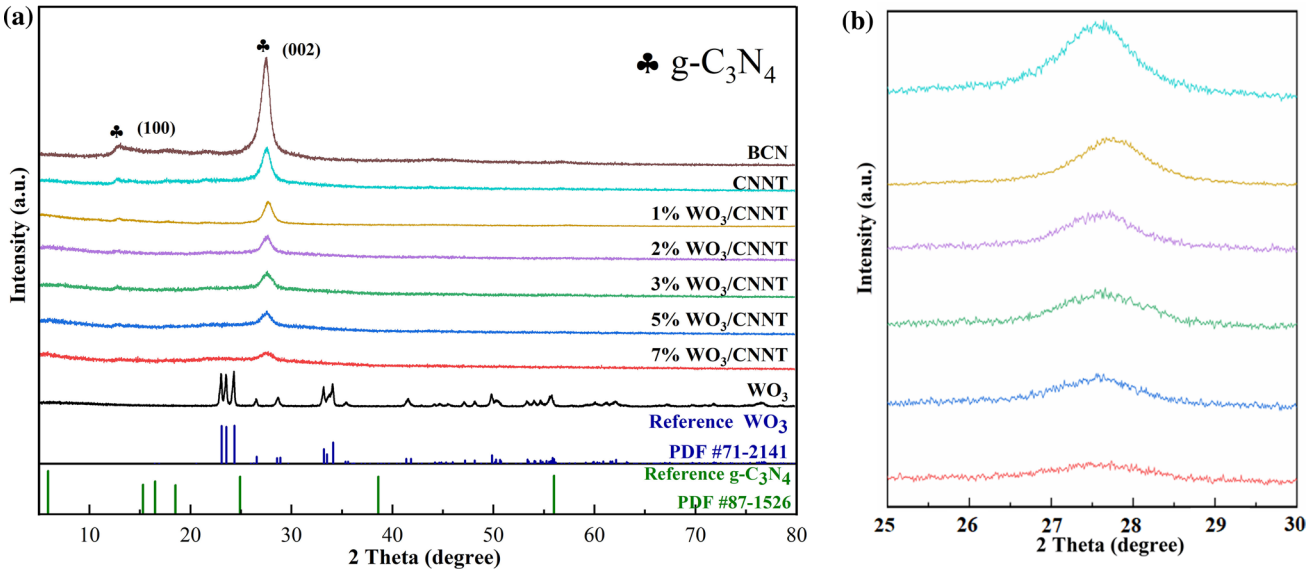

Fig. 1 (a) XRD patterns of pure WO_3, BCN and CNNT, and of the WO_3/CNNT composite samples, (b) magnified XRD patterns of the WO_3/CNNT samples.

27.8° (shown in Fig. 1a) as the (100) and (002) crystal facets (JCPDS No. 87–1526). The weaker diffraction peak at $2\theta = 13.5°$ corresponded to the in-plane structures of tri-s-triazine units, whereas a more prominent peak at $2\theta = 27.8°$ is associated with the interlayer packing.[35] However, the peak strength of CNNT is lower than that of BCN, indicating that the nanomaterial has obvious size dependence, and that tri-s-triazine building blocks have a shorter correlation length of interlayer periodicity.[36] There is no discernible peak of WO_3 in the composite materials, perhaps because of its low load. By magnifying the XRD figure $2\theta = 25°–30°$, shown in Fig. 1b, it is clear that, when the WO_3 loading increases, the reduction of the (002) crystal facets may be caused by the insertion of loaded WO_3 into the lattice of CNNT.

FT-IR Analysis

Figure 2 compares the FT-IR patterns of WO_3, CNNT, and 2% WO_3/CNNT composites at room temperature. The broad peak located at 450–900 cm^{-1} is attributed to the stretching vibration of W-O-W,[37] note the formation of a g-C_3N_4 phase in the CNNT and 2% WO_3/CNNT. The distinctive peak at 810 cm^{-1} is from the characteristic breathing vibration of the tri-s-triazine units.[38] Meanwhile, typical stretching modes of C-N and C=N groups were in the 1200–1700 cm^{-1} region. In addition, the peak at 3000–3400 cm^{-1} can be ascribed to the stretching vibration of -OH.[39,40]

Morphology

The microstructures of WO_3, BCN, CNNT, and 2% WO_3/CNNT were revealed by FE-SEM. According to Fig. 3a, the diameter of pure WO_3 nanoparticles is between 100 and 200 nm. It can be noted from Fig. 3b that the morphology of BCN is a block structure formed by a nanosheet assembly. As shown in Fig. 3c, the CNNT is a tubular structure with a diameter of about 300 nm. As seen from Fig. 3d, the 2% WO_3/CNNT exhibited a porous nanotube structure. During calcination, the mass of NH_3 and CO_2 were released, resulting in the characteristic porous structure. Figure 3e, f show the EDS spectra of 2% WO_3/CNNT. The existence of the Cu element is derived from the use of a Cu sheet as a carrier, clearly demonstrating that there are C, N, W, and O elements in the sample. The presence of impurities can act as the capture site of electrons–holes and lead to reducing the mobility of the charge.[41] Figure 3f further ratifies the absence of impurities in the sample. The EDS mapping images of the 2% WO_3/CNNT indicate the elemental composition of C, N, W, and O with homogeneous distribution in the composite, as shown in Fig. 3g–k. As can been seen from the TEM image in Fig. 4a, some WO_3 nanoparticles are thoroughly bound to the surface of the CNNT. Using HRTEM, the lattice fringes and interface between both components were observed. The HRTEM image of the composites in Fig. 4b reveals a close interface between the two components, supporting the heterojunction formation. The lattice spacing was about 0.202 nm, attributed to the (123) plane of WO_3. According to the above results, it can be easily concluded that the WO_3 and CNNT are compatible with a heterojunction through robust interface interactions.

XPS Surveys

The XPS survey (Fig. 5a) revealed that the 2% WO_3/CNNT composite is composed of C, N, W, and O elements, which is consistent with the EDS results. The C 1s spectrum (Fig. 5b) presents two principal peaks located at 284.8 eV and 288.4 eV, respectively, belonging to the sp^2 C-C bonds and the sp^2-hybridized N-C=N bonding. Furthermore, a weak peak at 286.3 eV is due to incomplete polymerization of terminal amino groups at the edge of heptazine units.[42] The N 1s spectrum (Fig. 5c) shows that there are four peaks, located at 398.5 eV, 399.2 eV, 400.9 eV, and 404.4 eV, originating from the C-N=C bond, N-$(C)_3$ bond, C-NH_2 bond, and the π-excitation of C-N heterocycles, respectively.[37] As shown in Fig. 5d, it is evident from the W 4f spectrum that there are two peaks with binding energies of 35.4 eV and 37.6 eV, attributed to W $4f_{5/2}$ and W $4f_{7/2}$, respectively.[43] The high-resolution O 1s spectra (Fig. 5e) exhibits two peaks, at 530.4 eV and 532.2 eV, with W-O-W bond ascribed to oxygen species in WO_3 and the other peak is adsorbed oxygen from g-C_3N_4.[44] Above all, the XPS analysis proves the introduction of WO_3 to CNNT in the 2% WO_3/CNNT composite.

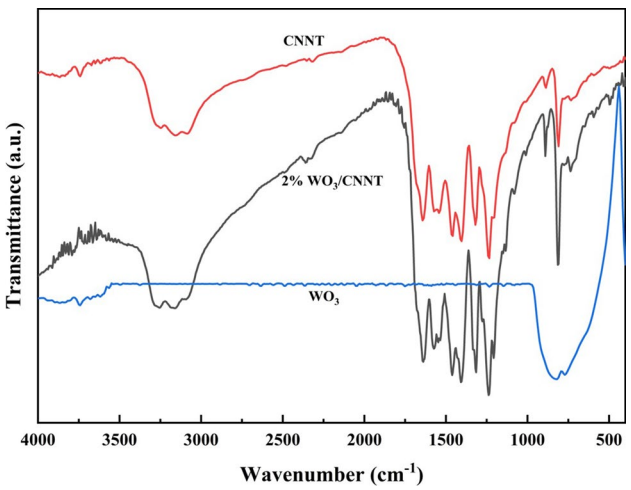

Fig. 2 FT-IR spectra of WO_3, CNNT and 2% WO_3/CNNT.

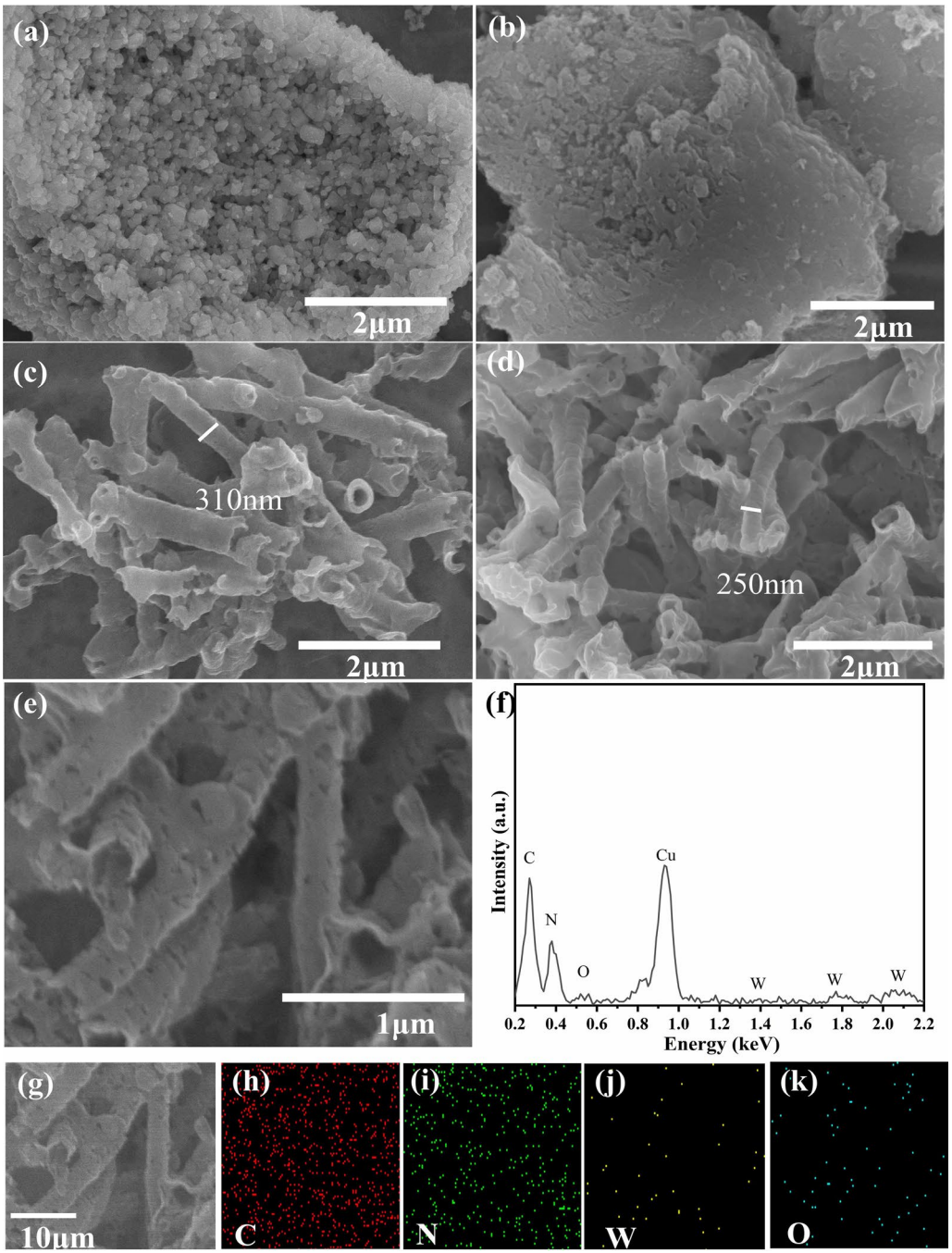

Fig. 3 FE-SEM micrographs of the samples: (a) WO_3; (b) BCN; (c) CNNT; (d) 2%WO_3/CNNT; (e) FE-SEM image and (f) EDS spectrum of 2%WO_3/CNNT; (g–k) FE-SEM image and the elemental mapping images of 2%WO_3/CNNT.

Specific Surface Area and Pore Structure

The nitrogen adsorption–desorption isotherms were studied, and the effects of morphology and doping WO_3 nanoparticles on the specific surface area and pore size of carbon nitride were also analyzed. As seen in Fig. 6a, the as-prepared catalyst exhibited a type IV adsorption–desorption isotherm with a H3 hysteresis loop, indicating that the sample has an obvious mesoporous structure.[45,46] Compared with the BCN, the CNNT has a more significant BET surface area (83.82 m^2/g), which is quite likely due to the fact that the hollow nanotube structure, richly endowed with a hierarchical pore structure obtained from supramolecular precursors, can increase the specific surface. Furthermore, the BET surface area of the 2% WO_3/CNNT nanotube composite was investigated and reached 108.82 m^2/g, larger than

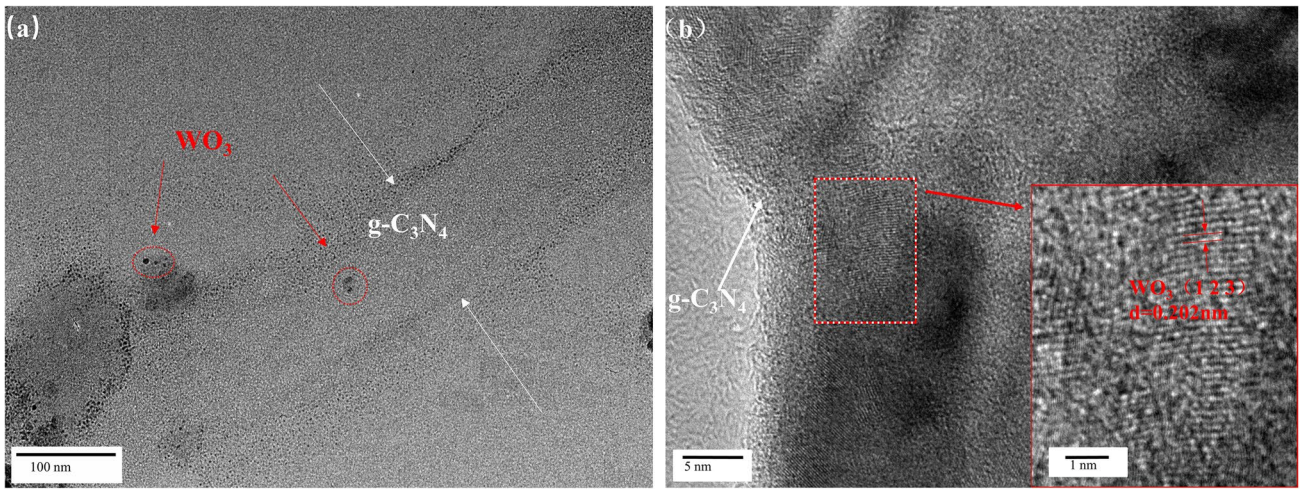

Fig. 4 (a) TEM and (b) HRTEM photo of 2% WO_3/CNNT; inset HRTEM.

that of a single g-C_3N_4 and WO_3, suggesting that composite materials can improve the surface area, thus providing more reaction and adsorption active sites in the photocatalytic process.[47,48] The pore size distribution of the composite belongs to a mesoporous structure, which is about 19.14 nm, much larger than that of the single material. The porous structure of the 2% WO_3/CNNT facilitates the complete absorbtion of light illuminating its surface and speeds up the mobility of reactants and products throughout the reaction process.

Optical Properties

UV–vis DRS analysis was used to study the optical absorption region of the BCN, CNNT, WO_3 and 2% WO_3/CNNT composite in the range of 300–600 nm. As shown in Fig. 7a, the BCN and CNNT display an absorption edge in the visible light region whereas WO_3 shows the strongest absorption at approximately 497 nm. The as-prepared binary composites exhibit a red shift and more significant UV and visible absorption than the BCN and CNNT, which may be attributed to the remarkable porous nanotube structure and coupling between WO_3 and g-C_3N_4. Upon irradiating nanocomposites with visible light, remarkable photocatalytic properties can be achieved by the high absorption in the visible region.

Generally, by using the Tauc plot method, a semiconductor photocatalyst's optical absorption edge (E_g) can be estimated:

$$\alpha h\nu = A(h\nu - E_g)^{n/2} \tag{1}$$

where the photon energy, light frequency, proportionality and band gap energy are represented by the absorption coefficients of α, h, ν, A, and E_g, respectively. The band gap energy for the CNNT was determined from a plot of $(\alpha h\nu)^2$ versus hv ($n = 4$), and the WO_3 was also calculated from a plot of $(\alpha h\nu)^2$ versus $h\nu$ ($n = 4$). The band gaps of CNNT and WO_3 are, respectively, estimated to be 3.01 eV and 2.66 eV (Fig. 7b), nearly the same as those previously reported.[49,50] In the composites, the band gap is between individual samples, which can explain the enhancement in light absorption.

Photoelectrochemical Measurements

Mott–Schottky Plots

An investigation of the band edge potentials and heterojunction formation has been conducted using Mott–Schottky plots. From Fig. 8a and b, the positive slope of the plots reveals that both WO_3 and CNNT are *n*-type semiconductors.[51] It was found that, for WO_3 and CNNT, the bandgap potentials were − 0.02 eV and − 1.2 eV (vs. Ag/AgCl, pH = 7), respectively. The following can be used to analyze the potentials of the conduction band (CB) (compared to a normal hydrogen electrode, NHE pH = 0):

$$E_{(NHE)} = E_{(Ag/AgCl)} + 0.197 \tag{2}$$

thus, the CB potentials of the WO_3 and CNNT are, respectively, estimated to be 0.18 eV and − 1.0 eV (vs. NHE). By further considering their E_g (Fig. 7b), the valence band (VB) potentials of the WO_3 and CNNT are, respectively, measured to be 2.84 eV and 2.01 eV (versus NHE) by applying:

$$E_{VB} = E_g + E_{CB} \tag{3}$$

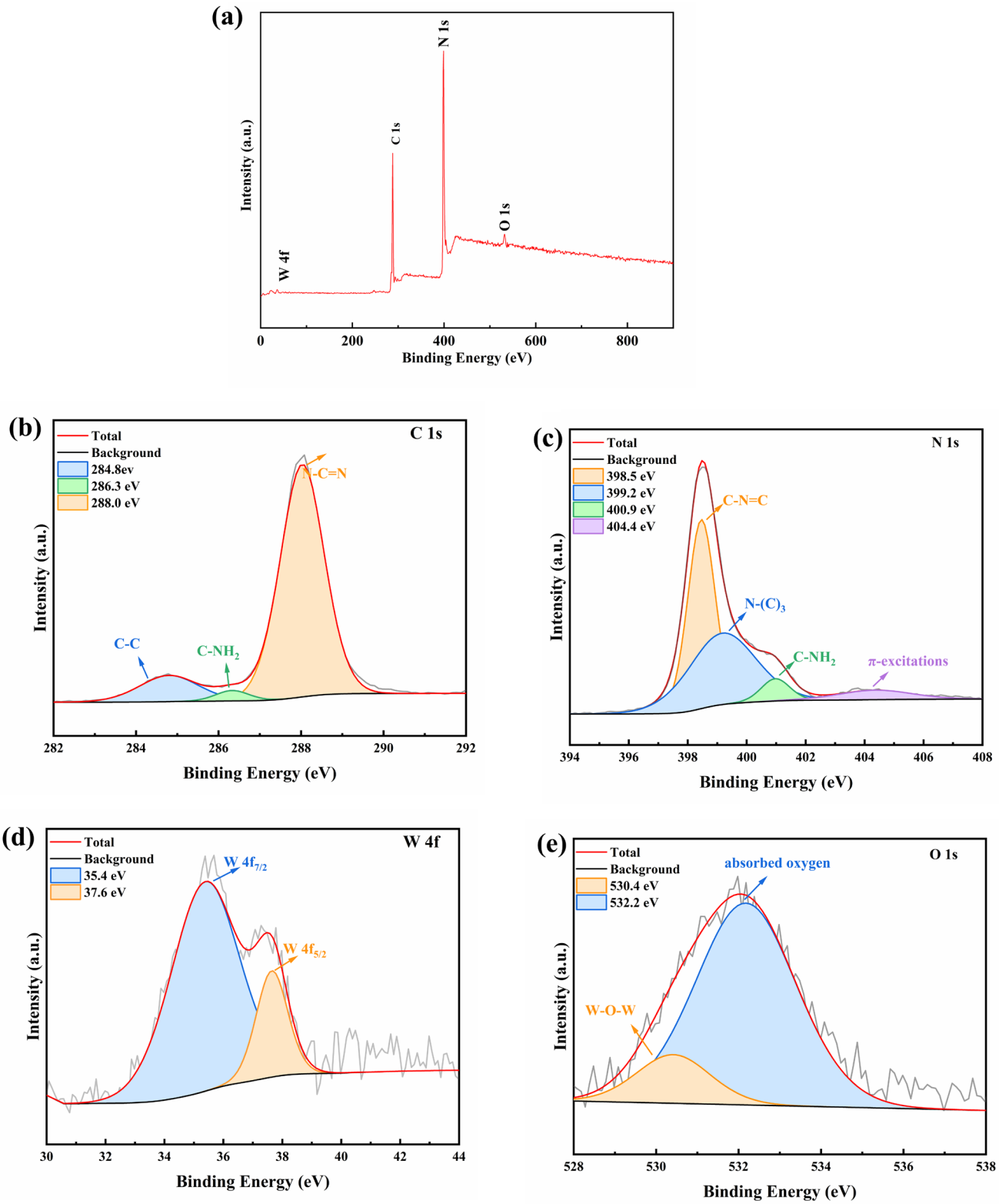

Fig. 5 (a) Total XPS survey of 2% WO_3/CNNT sample and the high-resolution spectra of (b) C 1*s*, (c) N 1*s*, (d) W 4*f*, and (e) O 1*s*.

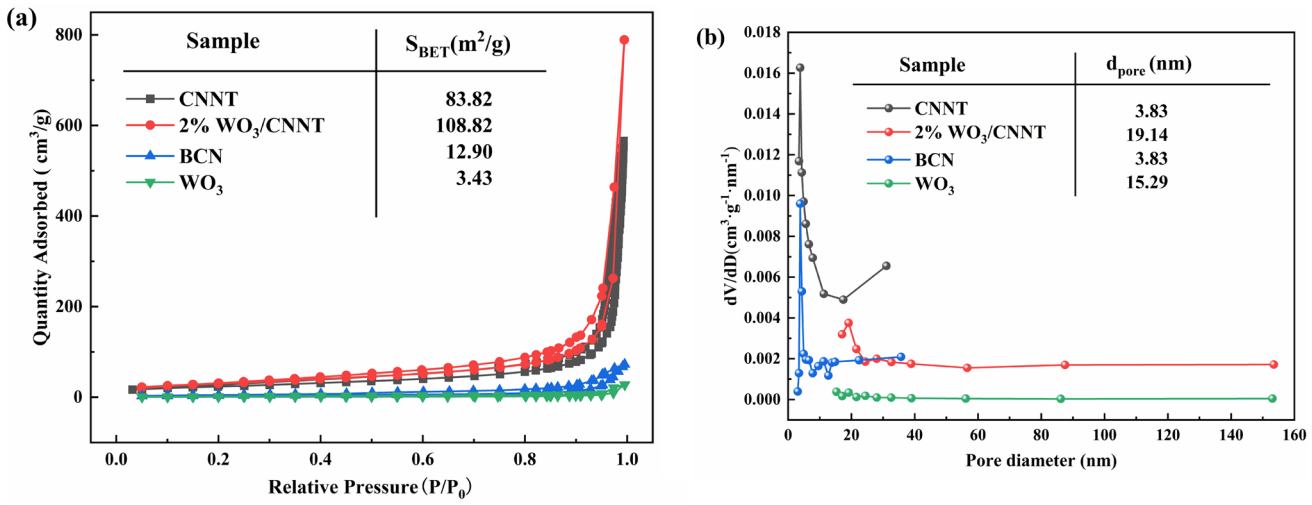

Fig. 6 (a) N_2 adsorption–desorption isotherms and (b) corresponding pore size distribution curves of the synthesized WO_3, BCN, and 2% WO_3/CNNT.

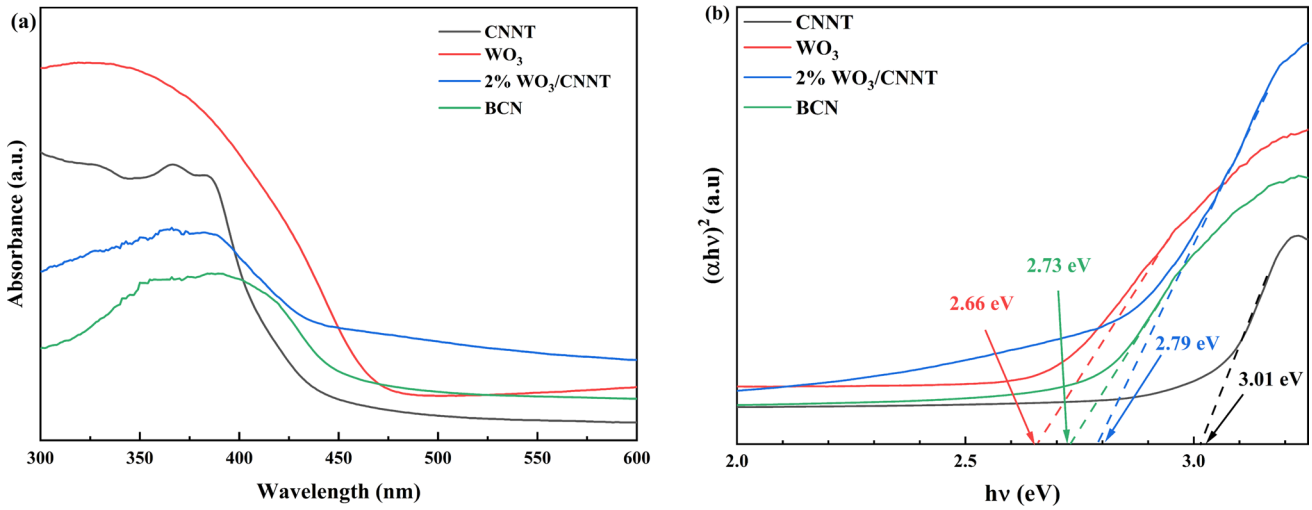

Fig. 7 (a) UV–vis diffuse reflectance spectra of WO_3, BCN, CNNT, and 2% WO_3/CNNT and (b) band gap energies of WO_3, BCN, CNNT, and 2% WO_3/CNNT.

Photocurrent Transient Response Tests

For the purpose of investigating electron transfer during the light-on and light-off modes of the composite system, photocurrent response tests were conducted as shown in Fig. 8c. After the catalysts had been irradiated, the photocurrent dramatically increased. However, the photocurrent rapidly decreased after the light was turned off. There was an obvious improvement in photocurrent intensities in the composites, and the course can be repeated continuously. According to the results, it can be seen that the WO_3 promotes the separation of electrons and holes by forming interfaces between the CNNT and the WO_3.

EIS Analysis

The EIS tests of the BCN, CNNT, pure WO_3 , and 2% WO_3/CNNT composite are set out in Fig. 8d. A comparison of the BCN and CNNT samples shows a large arc radius of Nyquist plots; however, for the 2% WO_3/CNNT composite, the arc radius clearly decreases, suggesting a better transport of charges. However, the radius of the Nyquist diagram of WO_3 sample is small. Therefore, the charge transfer rate in this composite system may not be a critical factor in high degradation efficiency.

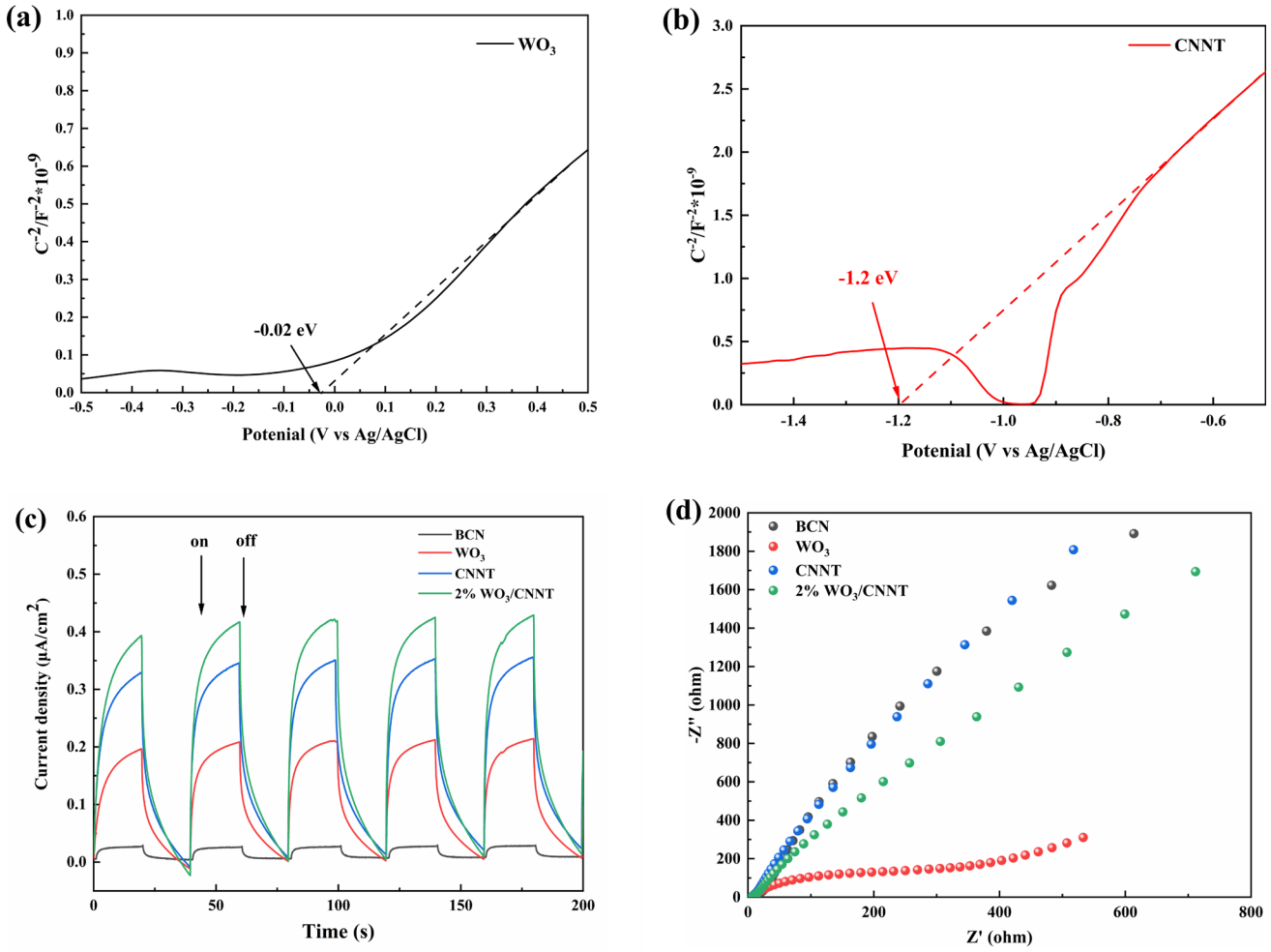

Fig. 8 Mott–Schottky plots: (a) WO_3 and (b) CNNT; (c) photocurrent responses and (d) EIS spectra of the samples under visible light.

Photocatalytic Properties of the Samples

As a representative dye for the photo-oxidation process, the RhB molecule (maximum absorption band at 554 nm) was employed to study the photocatalytic activity of the photocatalysts. As shown in Fig. 9a and b, the photocatalytic results indicated that pure WO_3 nanoparticles and BCN have insufficient degradation efficiency of RhB. However, the degradation efficiency of CNNT was significantly improved, indicating that morphology regulation could affect the degradation efficiency of g-C_3N_4. Additionally, under visible-light irradiation, the WO_3 doping significantly affected the WO_3/CNNT composite's photocatalyst performance, the 1%, 2%, 3%, and 5% WO_3/CNNT exhibiting higher photocatalytic efficiencies in degrading RhB compared with CNNT. This improvement of photocatalytic performance may be due to the enhancement of carrier separation efficiency. Among them, the 2% WO_3/CNNT is most prominent, with a high k value of 0.335 min^{-1}, which is 3.4 times greater than CNNT and 83.8 times greater than single WO_3. When the proportion of WO_3 was further increased to 7%, the photocatalytic activity decreased. It may be that the active site of CNNT is blocked by excessive WO_3 nanoparticles, and the photoadsorption sites of CNNT are covered. In Fig. 9c, the cyclic photocatalytic degradation tests were carried out with the 2% WO_3/CNNT composites. The RhB degradation rate only slightly declined, from 97.4% to 91.8%, during the course of the four cycles of the 2% WO_3/CNNT composite, revealing its excellent stability and reusability. The different scavengers (AO, BQ, DMSO, IPA) were taken to explore the impacts of the main active species during photocatalytic degradation of the RhB. The AO, BQ, DMSO, and IPA have been added for quenching the h^+, $\cdot O_2^-$, ·OH, and e^- radicals, respectively.[52,53] From Fig. 9d, it can be seen that the AO and BQ can more successfully inhibit the degradation process than DMSO and IPA during photocatalysis. The results identified in these responses are that the $\cdot O_2^-$ and h^+ radicals are the pivotal species in the total degradation process.

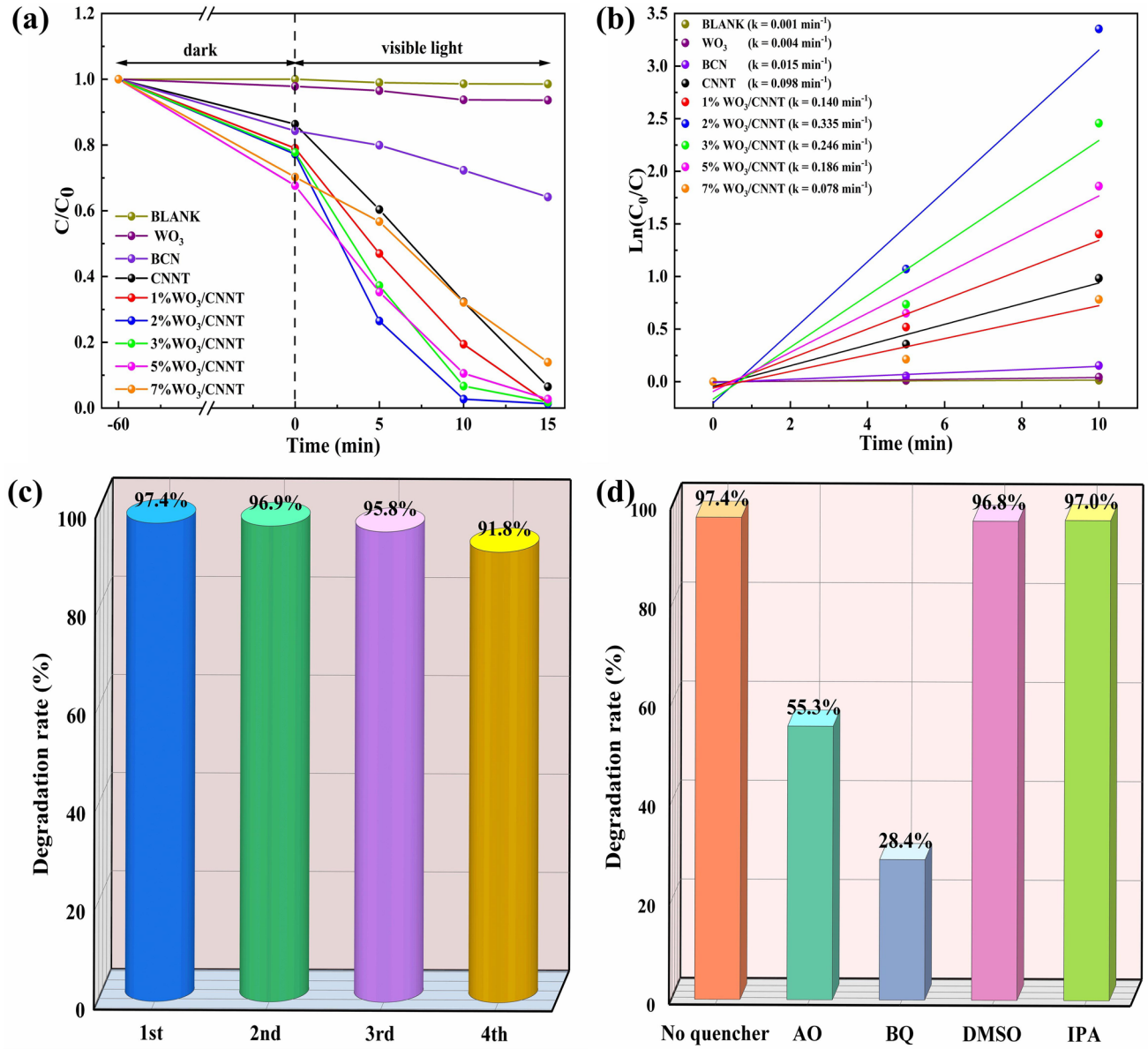

Fig. 9 (a) Photocatalytic RhB adsorption–degradation curves under visible-light irradiation of the synthesized photocatalysts; (b) pseudo-first-order kinetics plot for the RhB degradation over the as-prepared photocatalysts; (c) four cycles of 2% WO_3/CNNT for the degradation rate; and (d) photocatalytic RhB under visible-light irradiation degradation with different reactive species scavengers (AO, BQ, DMSO, IPA).

As shown in Fig. 10a, there was no apparent absorbance peak measured after 40 min of irradiation, indicating almost complete degradation of TC. As can be seen in Fig. 10b and c, the photocatalyst degradation rate of TC accorded with the following order: 2% WO_3 > CNNT > 1% WO_3 > 5% WO_3 > 3% WO_3 > 7% WO_3 > BCN > WO_3. Similarly, the k value of 2% WO_3/CNNT (0.043 min^{-1}) for TC degradation was about 1.1 times higher than CNNT (0.040 min^{-1}), and 14.3 times higher than pure WO_3 (0.003 min^{-1}). It can be seen in Fig. 10d that the synthesized catalysts can be used repeatedly for the treatment of antibiotic wastewater by photocatalysis. In Fig. 10e, the collected photocatalyst after the degradation process was characterized by XRD and compared with the composite photocatalyst before the photodegradation cycles. It can be seen that there are no obvious impurities and that the position of the peak remains unchanged. These complete structures imply that the WO_3/CNNT composite photocatalyst possesses excellent stability without apparent inactivation.

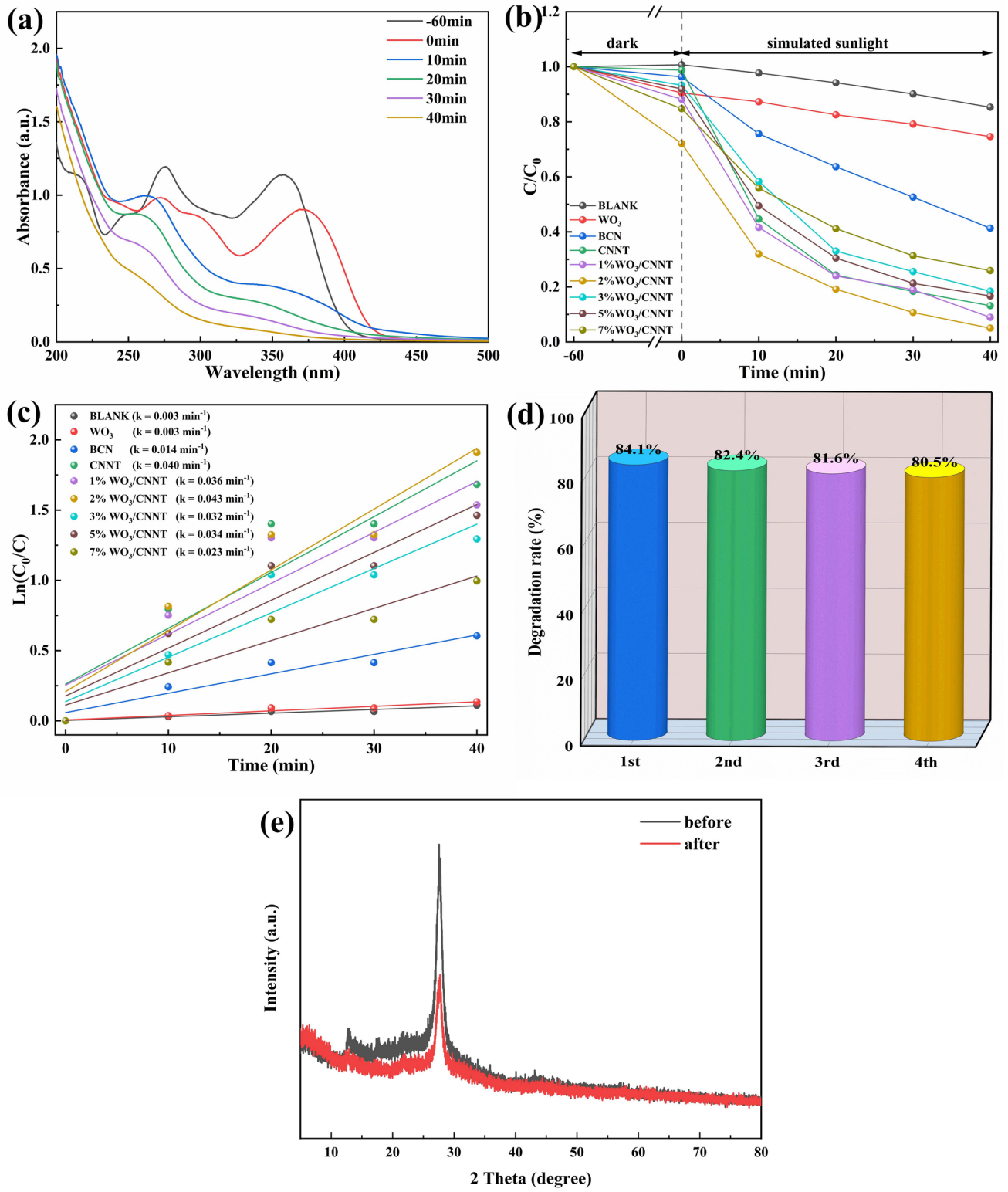

Fig. 10 (a) UV–vis spectra of TC solutions during photocatalytic treatment using the 2% WO_3/CNNT catalyst; (b) adsorption–degradation curves; (c) pseudo-first-order kinetics of samples; (d) photocatalytic TC stability test of the 2% WO_3/CNNT sample under simulated solar light; and (e) XRD patterns of before and after photodegradation cycles of the 2% WO_3/CNNT sample.

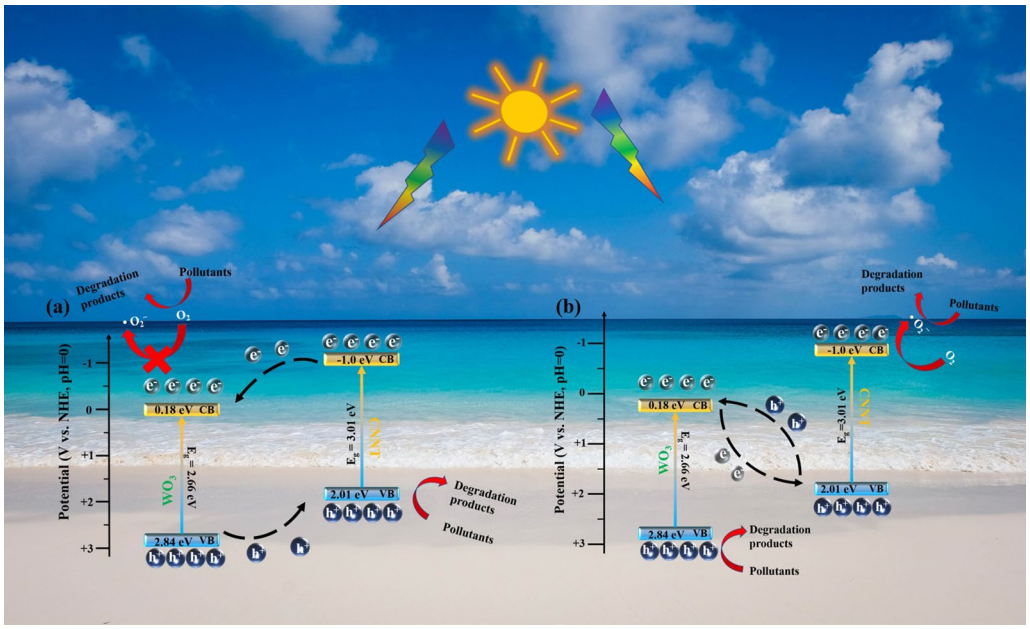

Scheme 2 The possible photocatalytic mechanism of the WO_3/g-C_3N_4 nanotubes: (a) double-charge transfer mechanism and (b) Z-scheme mechanism.

Table I Comparing the degradation performance of other g-C_3N_4-based heterojunction photocatalysts with previous examples

S. No.	Photocatalyst	Light source	Amount of photocatalyst (mg)	Pollutant	Degradation efficiency (%)	Rate constant (min^{-1})	Ref.
1	Porous tubular g-C_3N_4 capture black phosphorus quantum dots	300 W visible-light	30	Oxytetracycline hydrochloride (OTD-HCl)	81.05	0.0276	55
2	h-BN/g-C_3N_4	300 W visible-light	100	TC 10 mg/L	79.7	0.02775	56
3	Coral like WO_3/g-C_3N_4	65 W CFL lamp	5	Methylene blue	97.82	0.0419	43
4	$Fe_3N/Fe_2O_3/C_3N_4$	300 W visible-light	40	RhB	99.88	0.1	57
5	g-C_3N_4/diatomite/Fe_3O_4 composites	500 W visible-light	30	RhB	98	0.008	58
6	WO_3/g-C_3N_4 nanotubes	300 W visible-light	10	RhB	97.4	0.335	This work
6	WO_3/g-C_3N_4 nanotubes	300 W sunlight	20	TC	84.1	0.043	This work

Mechanism of Enhanced Photocatalytic Performance

The catalytic mechanism of RhB and TC degradation in the WO_3/g-C_3N_4 nanotube composites were inferred according to the above experimental results and discussion, as shown in Scheme 2. It is important to note that in most semiconductor heterojunction photocatalysts, there may be two general charge transfer routes (traditional band to band transfer and Z-type mechanisms) that will compete with each other. By utilizing the double-charge transfer mechanism (Scheme 2a), with sunlight illuminating the g-C_3N_4 nanotubes, electron–hole pairs are generated, and the electrons are transferred to the WO_3 nanoparticles as electron acceptors, owing to the potential of CB of WO_3 being below $O_2/\cdot O_2^-$ (− 0.33 eV) and the $\cdot O_2^-$ cannot be gained.[54] Therefore, we can surmise that the Z-scheme mechanism would be better matched to explain the charge separation process of the WO_3/CNNT nanotubes (Scheme 2b). Meanwhile, the photocatalysts consisting of one-dimensional tubes have higher charge carrier mobility along the longitudinal direction, which is beneficial for electron and hole separation and transfer, and can maximize the composites' exposure to light attributable to the incident light's several reflections. Finally, the obtained $\cdot O_2^-$ and h^+ can easily react with RhB (TC) molecule. A comparison of the degradation of various pollutants using different g-C_3N_4-based heterojunction

photocatalysts is presented in Table I. Based on these results, the synthesized WO_3/g-C_3N_4 composites can effectively remove RhB and TC from wastewater with outstanding photocatalytic properties.

Conclusions

A simple one-pot calcination method was used to successfully synthesize tubular g-C_3N_4 incorporated with WO_3 and examined for photocatalytic activity. For visible-light and sunlight degradation, the 2% WO_3/CNNT was believed to have the highest removal rate. Under visible light, the degradation efficiency of RhB solution reached 97.4% in 15 min, and the 84.1% TC solution can be degraded in 40 min under the condition of simulated sunlight. In addition, the reaction rate constant, k, reached 0.335 min^{-1} and 0.043 min^{-1}, respectively. The selectivity may be the reason for the different degradation efficiency of catalysts for different pollutants in sunlight and visible light. According to the active species trapping experimental results, the $\cdot O_2^-$ and h^+ radicals played crucial roles in the photocatalytic degradation of RhB in 2% WO_3/CNNT. The enhanced photocatalytic activity was due to the formation of the Z-scheme heterojunction between the WO_3 and g-C_3N_4, leading to a high surface area and light absorption capacity of the photocatalyst. The current work paves the way for the development of versatile g-C_3N_4-based heterojunction materials with a specific structure and an enhanced photocatalytic performance.

Acknowledgments This job is financially supported by the Natural Science Foundation of Anhui Province (Nos. 2008085QE277, 2208085QE137), the Natural Science Foundation of Education Department of Anhui Province (Nos. KJ2021A1018, KJ2021A0940), the National Natural Science Foundation of China (52075144) and the Graduate Innovation and Entrepreneurship Project of Hefei University (No. 21YCXL39).

Author Contributions HQ: writing—original draft, data curation; JL: resources; LG: investigation; ZZ: software; JZ: software; ZX: visualization; SW: software; TY: visualization; HL: validation; KH: funding acquisition; ML: methodology; JX: conceptualization, supervision, methodology.

Conflict of interest The authors declare that they have no known competing financial interests or personal relationships that could have appeared to influence the work reported in this paper.

References

1. L.P. Zhang, G.H. Wang, Z.Z. Xiong, H. Tang, and C.J. Jiang, Fabrication of flower-like direct Z-scheme β-Bi_2O_3/g-C_3N_4 photocatalyst with enhanced visible light photoactivity for Rhodamine B degradation. *Appl. Surf. Sci.* 436, 162 (2018).
2. J.F. Dai, X.F. Chen, and H. Yang, Visible light photocatalytic degradation of dyes by a new polyaniline/β-Bi_2O_3 composite. *Inorg. Nano-Met. Chem.* 47, 1364 (2017).
3. Y.L. Xu, X.F. Shi, R. Hua, R. Zhang, Y.J. Yao, B. Zhao, T. Liu, J.Z. Zheng, and G. Lu, Remarkably catalytic activity in reduction of 4-nitrophenol and methylene blue by Fe_3O_4@COF supported noble metal nanoparticles. *Appl. Catal. B Environ.* 260, 118142 (2020).
4. D. Li and W.D. Shi, Recent developments in visible-light photocatalytic degradation of antibiotics. *Chin. J. Catal.* 37, 792 (2016).
5. Y.P. Feng, G. Chen, Y.J. Zhang, D.G. Li, C. Ling, Q.Y. Wang, and G.G. Liu, Superhigh co-adsorption of tetracycline and copper by the ultrathin g-C_3N_4 modified graphene oxide hydrogels. *J. Hazard. Mater.* 424, 127362 (2022).
6. L.N. Fu, J. Li, G.Y. Wang, Y.N. Luan, and W. Dai, Adsorption behavior of organic pollutants on microplastics. *Ecotoxicol. Environ. Saf.* 217, 112207 (2021).
7. S. Lu, L.B. Liu, Q.X. Yang, H. Demissie, R.Y. Jiao, G.Y. An, and D.S. Wang, Removal characteristics and mechanism of microplastics and tetracycline composite pollutants by coagulation process. *Sci. Total Environ.* 786, 147508 (2021).
8. L.S. Copete-Pertuz, E.A. Serna-Galvis, J. Placido, R.A. Torres-Palma, and A.L. Mora-Martinez, Coupling chemical oxidation processes and *Leptosphaerulina* sp. myco-remediation to enhance the removal of recalcitrant organic pollutants in aqueous systems. *Sci. Total Environ.* 772, 145449 (2021).
9. S.K. Sahoo, S. Bhattacharya, and N.K. Sahoo, Photocatalytic degradation of biological recalcitrant pollutants: a green chemistry approach. *Biointerface Res. Appl. Chem.* 10, 5048 (2020).
10. H.P. Zhao, G.F. Li, F. Tian, Q.T. Jia, Y.L. Liu, and R. Chen, g-C_3N_4 surface-decorated $Bi_2O_2CO_3$ for improved photocatalytic performance: theoretical calculation and photodegradation of antibiotics in actual water matrix. *Chem. Eng. J.* 366, 468 (2019).
11. R. Jahanshahi, S. Sobhani, and J.M. Sansano, High performance magnetically separable G-C_3N_4/γ-Fe_2O_3/TiO_2 nanocomposite with boosted photocatalytic capability towards the Cefixime trihydrate degradation under visible-light. *ChemistrySelect* 5, 10114 (2020).
12. H.P. Li, Z. Wang, Y.X. Lu, S. Liu, X.J. Chen, G.Y. Wei, G. Ye, and J. Chen, Microplasma electrochemistry (MIPEC) methods for improving the photocatalytic performance of g-C_3N_4 in degradation of RhB. *Appl. Surf. Sci.* 531, 147307 (2020).
13. W. Wang, J.J. Fang, S.F. Shao, M. Lai, and C.H. Lu, Compact and uniform TiO_2@g-C_3N_4 core–shell quantum heterojunction for photocatalytic degradation of tetracycline antibiotics. *Appl. Catal. B Environ.* 217, 57 (2017).
14. M. Alhaddad, R.M. Navarro, M.A. Hussein, and R.M. Mohamed, Bi_2O_3/g-C_3N_4 nanocomposites as proficient photocatalysts for hydrogen generation from aqueous glycerol solutions beneath visible light. *Ceram. Int.* 46, 24873 (2020).
15. M. Zhou, S.B. Wang, P.J. Yang, Z.S. Luo, R.S. Yuan, A.M. Asiri, M. Wakeel, and X.C. Wang, Layered heterostructures of ultrathin polymeric carbon nitride and $ZnIn_2S_4$ nanosheets for photocatalytic CO_2 reduction. *Chem. Eur. J.* 24, 18529 (2018).
16. B.C. Zhu, P.F. Xia, W.K. Ho, and J.G. Yu, Isoelectric point and adsorption activity of porous g-C_3N_4. *Appl. Surf. Sci.* 344, 188 (2015).
17. Z.A. Hu, J.J. Zhou, Y.J. Ai, L. Liu, L. Qi, R.H. Jiang, H.J. Bao, J.T. Wang, J.S. Hu, H.B. Sun, and Q.L. Liang, Two dimensional Rh/Fe_3O_4/g-C_3N_4-N enabled hydrazine mediated catalytic transfer hydrogenation of nitroaromatics: a predictable catalyst model with adjoining Rh. *J. Catal.* 368, 20 (2018).
18. X.C. Wang, K. Maeda, A. Thomas, K. Takanabe, G. Xin, J.M. Carlsson, K. Domen, and M. Antonietti, A metal-free polymeric

photocatalyst for hydrogen production from water under visible light. *Nat. Mater.* 8, 76 (2009).
19. M. Chen, C.S. Guo, S. Hou, J.P. Lv, Y. Zhang, H. Zhang, and J. Xu, A novel Z-scheme AgBr/P-g-C_3N_4 heterojunction photocatalyst: excellent photocatalytic performance and photocatalytic mechanism for ephedrine degradation. *Appl. Catal. B Environ.* 266, 118614 (2020).
20. A.N. Shafawi, R.A. Mahmud, K. Ahmed Ali, L.K. Putri, N.I. Md Rosli, and A.R. Mohamed, Bi_2O_3 particles decorated on porous g-C_3N_4 sheets: enhanced photocatalytic activity through a direct Z-scheme mechanism for degradation of reactive black 5 under UV–vis light. *J. Photochem. Photobiol. Chem.* 389, 112289 (2020).
21. W. Wang, J.J. Fang, S.F. Shao, M. Lai, and C.H. Lu, Compact and uniform TiO_2@g-C_3N_4 core-shell quantum heterojunction for photocatalytic degradation of tetracycline antibiotics. *Appl. Catal. B Environ.* 217, 57 (2017).
22. S. Ghafoor, A. Inayat, F. Aftab, H. Duran, K. Kirchhoff, S. Waseem, and S.N. Arshad, TiO_2 nanofibers embedded with g-C_3N_4 nanosheets and decorated with Ag nanoparticles as Z-scheme photocatalysts for environmental remediation. *J. Environ. Chem. Eng.* 7, 103452 (2019).
23. Q.Q. Liu, C.Y. Fan, H. Tang, X.J. Sun, J. Yang, and X.N. Cheng, One-pot synthesis of g-C_3N_4/V_2O_5 composites for visible light-driven photocatalytic activity. *Appl. Surf. Sci.* 358, 188 (2015).
24. S.V.P. Vattikuti, A.K.R. Police, J. Shim, and C. Byon, In situ fabrication of the Bi_2O_3-V_2O_5 hybrid embedded with graphitic carbon nitride nanosheets: oxygen vacancies mediated enhanced visible-light-driven photocatalytic degradation of organic pollutants and hydrogen evolution. *Appl. Surf. Sci.* 447, 740 (2018).
25. M.F. Lu, Q.Q. Li, C.L. Zhang, X.X. Fan, L. Li, Y.M. Dong, G.Q. Chen, and H.F. Shi, Remarkable photocatalytic activity enhancement of CO_2 conversion over 2D/2D g-C_3N_4/$BiVO_4$ Z-scheme heterojunction promoted by efficient interfacial charge transfer. *Carbon* 160, 342 (2020).
26. Y.L. Tian, B.B. Chang, J.L. Lu, J. Fu, F.N. Xi, and X.P. Dong, Hydrothermal synthesis of graphitic carbon nitride–Bi_2WO_6 heterojunctions with enhanced visible light photocatalytic activities. *ACS Appl. Mater. Interfaces* 5, 7079 (2013).
27. D.B. Wang, X. Yu, Q.G. Feng, X.H. Lin, Y. Huang, X.Q. Huang, X. Li, K. Chen, B.H. Zhao, and Z. Zhang, In-situ growth of β-Bi_2O_3 nanosheets on g-C_3N_4 to construct direct Z-scheme heterojunction with enhanced photocatalytic activities. *J. Alloys Compd.* 859, 157795 (2021).
28. Y. Wang, Z.S. Zheng, Y.L. Li, P.W. Jia, and T. Liu, Study on photocatalytic activity of Ag_2O modified BiOI/g-C_3N_4 composite photocatalyst for degradation of RhB. *J. Electron. Mater.* 51, 5508 (2022).
29. Y. Liang, W.C. Xu, J.Z. Fang, Z. Liu, D.D. Chen, T. Pan, Y.T. Yu, and Z.Q. Fang, Highly dispersed bismuth oxide quantum dots/graphite carbon nitride nanosheets heterojunctions for visible light photocatalytic redox degradation of environmental pollutants. *Appl. Catal. B Environ.* 295, 120279 (2021).
30. M.J. Liao, L. Su, Y.C. Deng, S. Xiong, R.D. Tang, Z.B. Wu, C.X. Ding, L.H. Yang, and D.X. Gong, Strategies to improve WO_3-based photocatalysts for wastewater treatment: a review. *J. Mater. Sci.* 56, 14416 (2021).
31. M.M. Zhang, Y.Y. Zhu, W.J. Li, F.Z. Wang, H.D. Li, X.T. Liu, W.W. Zhang, and C.J. Ren, Double Z-scheme system of silver bromide@bismuth tungstate/tungsten trioxide ternary heterojunction with enhanced visible-light photocatalytic activity. *J. Colloid Interface Sci.* 509, 18 (2018).
32. T.T. Xiao, Z. Tang, Y. Yang, L.Q. Tang, Y. Zhou, and Z.G. Zou, In situ construction of hierarchical WO_3/g-C_3N_4 composite hollow microspheres as a Z-scheme photocatalyst for the degradation of antibiotics. *Appl. Catal. B-Environ.* 220, 417 (2018).
33. T. Pan, D.D. Chen, W.C. Xu, J.Z. Fang, S.X. Wu, Z. Liu, K. Wu, and Z.Q. Fang, Anionic polyacrylamide-assisted construction of thin 2D–2D WO_3/g-C_3N_4 Step-scheme heterojunction for enhanced tetracycline degradation under visible light irradiation. *J. Hazard. Mater.* 393, 122366 (2020).
34. Y.Y. Yang, B.Y. Liu, J.Y. Xu, Q.Y. Wang, X. Wang, G.J. Lv, and J.H. Zhou, The synthesis of h-BN-Modified Z-Scheme WO_3/g-C_3N_4 heterojunctions for enhancing visible light photocatalytic degradation of tetracycline pollutants. *ACS Omega* 7, 1 (2022).
35. F.L. Wang, Y.F. Wang, Y.P. Feng, Y.Q. Zeng, Z.J. Xie, Q.X. Zhang, Y.H. Su, P. Chen, Y. Liu, K. Yao, W.Y. Lv, and G.G. Liu, Novel ternary photocatalyst of single atom-dispersed silver and carbon quantum dots co-loaded with ultrathin g-C_3N_4 for broad spectrum photocatalytic degradation of naproxen. *Appl. Catal. B Environ.* 221, 510 (2018).
36. J.S. Zhang, M.W. Zhang, C. Yang, and X.C. Wang, Nanospherical carbon nitride frameworks with sharp edges accelerating charge collection and separation at a soft photocatalytic interface. *Adv. Mater.* 26, 4121 (2014).
37. J.W. Fu, Q.L. Xu, J.X. Low, C.J. Jiang, and J.G. Yu, Ultrathin 2D/2D WO_3/g-C_3N_4 step-scheme H_2-production photocatalyst. *Appl. Catal. B Environ.* 243, 556 (2019).
38. G.Z. Sun, Q.Z. Gao, S.N. Tang, R.Z. Ling, Y. Cai, C. Yu, H. Liu, H.J. Gao, X.X. Zhao, and A.R. Wang, Fabrication and enhanced photocatalytic activity of *p–n* heterojunction $CoWO_4$/g-C_3N_4 photocatalysts for methylene blue degradation. *J. Electron. Mater.* 51, 3205 (2022).
39. Z.S. Wu, X.F. He, Y.T. Xue, X. Yang, Y.F. Li, Q.B. Li, and B. Yu, Cyclodextrins grafted MoS_2/g-C_3N_4 as high-performance photocatalysts for the removal of glyphosate and Cr (VI) from simulated agricultural runoff. *Chem. Eng. J.* 399, 125747 (2020).
40. F. Sun, D. Xu, Y.R. Xie, F. Liu, W.L. Wang, H. Shao, Q.L. Ma, H. Yu, W.S. Yu, and X.T. Dong, Tri-functional aerogel photocatalyst with an S-scheme heterojunction for the efficient removal of dyes and antibiotic and hydrogen generation. *J. Colloid Interface Sci.* 628, 614 (2022).
41. H. Sepahvand, and S. Sharifnia, Photocatalytic overall water splitting by Z-scheme g-C_3N_4/$BiFeO_3$ heterojunction. *Int. J. Hydrogen Energy* 44, 23658 (2019).
42. S.S. Li, Y.N. Peng, C. Hu, and Z.H. Chen, Self-assembled synthesis of benzene-ring-grafted g-C_3N_4 nanotubes for enhanced photocatalytic H_2 evolution. *Appl. Catal. B Environ.* 279, 119401 (2020).
43. J. Singh, A. Arora, and S. Basu, Synthesis of coral like WO_3/g-C_3N_4 nanocomposites for the removal of hazardous dyes under visible light. *J. Alloys Compd.* 808, 151734 (2019).
44. X.Y. Zhang, X.Y. Wang, J.Q. Meng, Y.Q. Liu, M. Ren, Y.H. Guo, and Y.X. Yang, Robust Z-scheme g-C_3N_4/WO_3 heterojunction photocatalysts with morphology control of WO_3 for efficient degradation of phenolic pollutants. *Sep. Purif. Technol.* 255, 117693 (2021).
45. F. Guo, X.L. Huang, Z.H. Chen, H.R. Sun, and L.Z. Chen, Prominent co-catalytic effect of CoP nanoparticles anchored on high-crystalline g-C_3N_4 nanosheets for enhanced visible-light photocatalytic degradation of tetracycline in wastewater. *Chem. Eng. J.* 395, 125118 (2020).
46. L.B. Jiang, X.Z. Yuan, G.M. Zeng, J. Liang, X.H. Chen, H.B. Yu, H. Wang, Z.B. Wu, J. Zhang, and T. Xiong, In-situ synthesis of direct solid-state dual Z-scheme WO_3/g-C_3N_4/Bi_2O_3 photocatalyst for the degradation of refractory pollutant. *Appl. Catal. B Environ.* 227, 376 (2018).
47. C.M. Li, G. Chen, J.X. Sun, Y.J. Feng, J.J. Liu, and H.J. Dong, Ultrathin nanoflakes constructed erythrocyte-like Bi_2WO_6 hierarchical architecture via anionic self-regulation strategy for

improving photocatalytic activity and gas-sensing property. *Appl. Catal. B Environ.* 163, 415 (2015).
48. S.E. Guo, Y.Q. Tang, Y. Xie, C.G. Tian, Q.M. Feng, W. Zhou, and B.J. Jiang, P-doped tubular g-C_3N_4 with surface carbon defects: universal synthesis and enhanced visible-light photocatalytic hydrogen production. *Appl. Catal. B Environ.* 218, 664 (2017).
49. Y.X. Zhu, Y. Feng, S.L. Chen, M.L. Ding, and J.F. Yao, Carbon nitride nanotube-based materials for energy and environmental applications: a review of recent progresses. *J. Mater. Chem. A.* 8, 25626 (2020).
50. L. Zhou, Y.F. Li, S.J. Yang, M. Zhang, Z.S. Wu, R.X. Jin, and Y. Xing, Preparation of novel 0D/2D Ag_2WO_4/WO_3 Step-scheme heterojunction with effective interfacial charges transfer for photocatalytic contaminants degradation and mechanism insight. *Chem. Eng. J.* 420, 130361 (2021).
51. Y.Z. Hong, C.S. Li, B.X. Yin, D. Li, Z.Y. Zhang, B.D. Mao, W.Q. Fan, W. Gu, and W.D. Shi, Promoting visible-light-induced photocatalytic degradation of tetracycline by an efficient and stable beta-Bi_2O_3@g-C_3N_4 core/shell nanocomposite. *Chem. Eng. J.* 338, 137 (2018).
52. F. Guo, W.L. Shi, W.S. Guan, H. Huang, and Y. Liu, Carbon dots/g-C_3N_4/ZnO nanocomposite as efficient visible-light driven photocatalyst for tetracycline total degradation. *Sep. Purif. Technol.* 173, 295 (2017).
53. G. Fan, Z.Y. Ma, X.B. Li, and L.J. Deng, Coupling of Bi_2O_3 nanoparticles with g-C_3N_4 for enhanced photocatalytic degradation of methylene blue. *Ceram. Int.* 47, 5758 (2021).
54. W. Guo, K. Fan, J.J. Zhang, and C.J. Xu, 2D/2D Z-scheme Bi_2WO_6/porous-g-C_3N_4 with synergy of adsorption and visible-light-driven photodegradation. *Appl. Surf. Sci.* 447, 125 (2018).
55. W.J. Wang, Q.Y. Niu, G.M. Zeng, C. Zhang, D.L. Huang, B.B. Shao, C.Y. Zhou, Y. Yang, Y.X. Liu, H. Guo, W.P. Xiong, L. Lei, S.Y. Liu, H. Yi, S. Chen, and X. Tang, 1D porous tubular g-C_3N_4 capture black phosphorus quantum dots as 1D/0D metal-free photocatalysts for oxytetracycline hydrochloride degradation and hexavalent chromium reduction. *Appl. Catal. B Environ.* 273, 119051 (2020).
56. L.B. Jiang, X.Z. Yuan, G.M. Zeng, Z.B. Wu, J. Liang, X.H. Chen, L.J. Leng, H. Wang, and H. Wang, Metal-free efficient photocatalyst for stable visible-light photocatalytic degradation of refractory pollutant. *Appl. Catal. B Environ.* 221, 715 (2018).
57. M. Padervand, B. Rhimi, and C.Y. Wang, One-pot synthesis of novel ternary $Fe_3N/Fe_2O_3/C_3N_4$ photocatalyst for efficient removal of Rhodamine B and CO_2 reduction. *J. Alloys Compd.* 852, 156955 (2021).
58. C.Y. Xiong, Q.F. Ren, X.Y. Liu, Z. Jin, Y. Ding, H.T. Zhu, J.P. Li, and R.R. Chen, Fenton activity on RhB degradation of magnetic g-C_3N_4/diatomite/Fe_3O_4 composites. *Appl. Surf. Sci.* 543, 148844 (2021).